Materials Advances

Accepted Manuscript

This is an Accepted Manuscript, which has been through the Royal Society of Chemistry peer review process and has been accepted for publication.

Accepted Manuscripts are published online shortly after acceptance, before technical editing, formatting and proof reading. Using this free service, authors can make their results available to the community, in citable form, before we publish the edited article. We will replace this Accepted Manuscript with the edited and formatted Advance Article as soon as it is available.

You can find more information about Accepted Manuscripts in the Information for Authors.

Please note that technical editing may introduce minor changes to the text and/or graphics, which may alter content. The journal's standard Terms & Conditions and the Ethical guidelines still apply. In no event shall the Royal Society of Chemistry be held responsible for any errors or omissions in this Accepted Manuscript or any consequences arising from the use of any information it contains.

Design and Optimization of Polyindole-Integrated Bimetallic Composites (PLN/CuO-NiO and PLN/Mn-Cu) for Efficient Photocatalytic Degradation of Imidacloprid under Sunlight Irradiation

Muhammad Imran[1], Amina Khan[1], Raheeba Akbar[1], Haq Nawaz Bhatti[1], Norah Alwadai[2] and Munawar Iqbal[3,*]

[1]Department of Chemistry, University of Agriculture, Faisalabad, Pakistan

[2]Department of Physics, College of Sciences, Princess Nourah bint Abdulrahman University, P.O. Box 84428, Riyadh 11671, Saudi Arabia

[3]School of Chemistry, University of Punjab, Lahore, Pakistan

*Corresponding author: Munawar.chem@pu.edu.pk

Abstract

The present study demonstrated the fabrication of novel polyindole (PLN) based-bimetallic nanocomposites (PLN/Mn-Cu and PLN/CuO-NiO) via coprecipitation, hydrothermal, and in-situ polymerization methods, for the photodegradation of imidacloprid (IMI) pesticide. Fourier transform infrared spectroscopy showed that PLN were successfully loaded onto the bimetallic nanocomposites' surface. X-ray diffraction analysis revealed that PLN/Mn–Cu exhibited a cubic phase with a crystallite size of 75 nm, while PLN/CuO–NiO retained cubic CuO and monoclinic NiO phases with a size of 54 nm. Scanning electron microscopy analysis showed that PLN/CuO–NiO featured spherical but irregular structures, while PLN/Mn–Cu exhibited a granular and uneven surface morphology. UV–visible analysis showed band gaps of 2.15 eV (PLN/Mn–Cu) and 2.13 eV (PLN/CuO–NiO), with strong absorption between 250–350 nm, confirming their visible-light photocatalytic potential. Photocatalytic activity of PLN/Mn–Cu and PLN/CuO–NiO composites exhibited a 91 and 98 % degradation efficiency of IMI pesticide under optimum conditions of pH = 10 and 4, catalyst dose = 5 mg/L, irradiation time = 120 min and 60 min, and pesticide dose = 2 and 6 mg/L, respectively. The kinetic study showed that the Behnajady-Modirshala-Ghanbery model fitted best to the experimental data. The study on reusability showed that catalysts can be used in five consecutive cycles. The work also demonstrates a sustainable and promising route for designing PLN-functionalized bimetallic nanocomposites for environmental remediation applications.

1. Introduction

Water is a vital and irreplaceable resource for sustaining life on Earth. Human activities at every stage of development rely heavily on water, making it an essential element for growth and well-being, which resultantly are contaminating the water resources. There has been rapid pollution of surface and groundwater during the last few years. One of the global challenges of the 21st century is the rapid increase in population, expanding industrialisation, growing urbanisation, and increasing agricultural practices, all of which contribute to a serious decline in superior water sources and lead to enormous wastewater production.[1] The major area in the world triggering water pollution is industrialization, discharging a large number of chemosynthetic materials with complex structures and high chemical stability into the water sources.[2] These waste materials are harmful to aquatic life and human beings, especially when they encompass materials such as heavy metals, pesticides, pharmaceutical products and dyes, because they alter the pH and chemical composition of water and disturb the environmental balance.[3]

There is a high demand for pesticides worldwide as a consequence of growing agricultural activities, abolition of numerous infectious diseases and improvement in personal hygiene. Pesticides are classified as fungicides, nematicides, insecticides, rodenticides, weedicides, herbicides, algaecides, and bactericides, but herbicides and insecticides are 77 % of the total pesticide usage in the world.[4] Of the 3.5 million tons of pesticides used throughout the world in a year.[5] Only 1 % reaches the target point and the remaining 99 % pollutes the soil, land and enters water resources through runoff and drainage.[6] Pesticides are causing a serious threat to aquatic life and humans, such as cancer, neurological disorders, diabetes mellitus, cardiovascular disorders, reproductive syndromes and respiratory disorders, because these mainly contain phenolic compounds in their composition, which are carcinogenic and mutagenic.[7]

Due to good environmental compatibility, a broad spectrum of efficacy and targeted insecticidal toxicity, the most widely used group of pesticides is neonicotinoid insecticides.[8] Neonicotinoid insecticides are composed of two main compounds, nitro-substituted compounds (Imidacloprid, clothianidin, thiamethoxam) and cyano-substituted compounds (thiacloprid and

acetamiprid).[9] Imidacloprid (IMI) is one of the most common neonicotinoid insecticides and its IUPAC name is 1-(6-chloro-3-pyridylmethyl)-N-nitroimidazolidin-2ylideneamine ($C_9H_{10}ClN_5O_2$).[10] IMI is the most chosen, as the first neonicotinoid insecticide and one of the extensively used chlorinated organic pesticides in the world.[11] This pesticide contains 140 agricultural products and is most commonly used to control insects, and pests in agriculture, landscaping, controlling termites and sucking insects, in grassland and livestock in more than 120 countries in the world since its synthesis.[12] IMI is readily soluble in water (0.58 g/L), has more than 30 days of stability, high photocatalytic removal, good environmental compatibility and higher toxicity. IMI has two half-life spans, aerobic and anaerobic. The aerobic half-life is 2-3 hours and the anaerobic half-life period is approximately 10-50 hours.[13] IMI accumulation is noticed in surface water, wastewater with higher concentrations and in low concentrations in human beings. So, it can affect the food chain and create a serious threat to human health, such as cramps, fatigue, twitching and muscle weakening.[14] It is necessary to pass such pesticide pollutants from sewage before releasing them into the water resources.

Conventional techniques have been adopted in treating pesticides pollutants are ozonolysis [15], biological treatment [16], sedimentation [17], reverse osmosis [18], chlorination [19], activated carbon adsorption [20], and filtration [21] etc., but these methods have limitations in remediation process such as low efficacy, hazardous byproduct formation, incomplete removal of pollutant, high energy consumption and high cost of maintenance etc.[22] However, recent technology has proposed the use of advanced oxidation processes (AOPs) such as photocatalysis to generate reactive oxygen species in the presence of daylight and semiconducting material for photo-degrading organic pollutants into H_2O, CO_2 and inorganic ions.[23] With photocatalysis, the combination of two divergent metals to form a bimetallic nanocomposite (BNC) results in remarkable properties, e.g., large surface area and reactivity, antibacterial property, nanosize and greater ability to catalyze reactions. Among the numerous semiconductors-based BNCs, use of transition metals and their oxides such as copper oxide nickel oxide (CuO-NiO), and manganese copper (Mn-Cu) with incorporation of polyindole (PLN) to form PLN/ CuO-NiO and PLN/ Mn-Cu, respectively, due to their low band gap (2.13 eV), large surface area, improved catalytic activity, enhanced electrical and optical properties in the field of photocatalysis.[24]

Among various types of conducting polymers, PLN has displayed tremendous consideration during the last few years, especially due to its superior environmental stability, thermal stability, chemical stability, and one-dimensional nanostructure, and is considered a promising candidate for redox reactions compared to other polymers.[25] This polymer is excellent in applications in electronics, sensors, batteries, catalysis and coating.[26] Various approaches have been used to synthesize these nanocomposites, including precipitation [27], hydrothermal methods [28] and in situ polymerization. [29] These synthesis methods are proven to be a cost-effective, efficient procedure, eco-friendly and do not use any hazardous solvents. Thus, the present research has been designed to enhance the photocatalytic activity of Mn-Cu and CuO-NiO by reducing their band gap by modification with conducting polymer PLN. To be specific, Mn-Cu was prepared by the hydrothermal method, CuO-NiO was synthesized via the precipitation method, and PLN was synthesized and loaded on the surface of these BNCs using the in-situ polymerization technique and employed for photodegradation of IMI in aqueous media (Fig. 1).
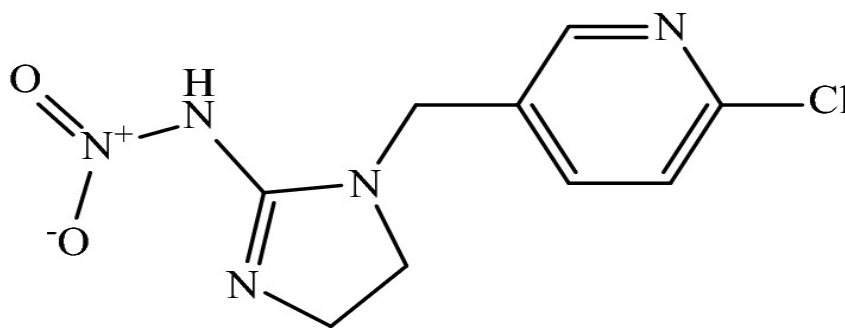

Fig. 1. Structure of Imidacloprid

2. Materials and methods

2.1 Materials

Copper nitrate trihydrate ($Cu(NO_3)_2.3H_2O$, 99%), nickel nitrate hexahydrate ($Ni(NO_3)_2.6H_2O$, 98%), zinc nitrate hexahydrate ($Zn(NO_3)_2.6H_2O$, 98%), ferric chloride hexahydrate ($FeCl_3.6H_2O$, 99%), sodium hydroxide (NaOH, 99%), indole (C_8H_7N, ≥ 98%) were purchased from Sigma-Aldrich (USA). Hydrochloric acid (HCl, 35%), ethanol (C_2H_5OH, ≥ 99%), methanol (CH_3OH, 99.8%) and potassium permanganate ($KMnO_4$, 99-100%) were procured from

Merck (Germany) and citric acid monohydrate ($C_6H_8O_7.H_2O$, 99.5%) was supplied by TTCA Co., ltd (China). The analytical grade imidacloprid (IMI; $C_9H_{10}ClN_5O_2$, Mw = 255.7 g/mol, 98%) pesticide was obtained from Sigma-Aldrich (USA). All these analytical-grade chemicals were used without doing any further sanitization.

2.2 Synthesis of PLN/CuO-NiO

The co-precipitation procedure was used to prepare CuO-NiO BNC. In the procedure, 0.2 M (40 mL) copper nitrate trihydrate solution was dissolved in 0.2 M (40 mL) nickel nitrate hexahydrate solution under magnetic stirring. Afterwards, 40 mL of 0.04 M citric acid monohydrate solution was made in deionized (DI) water and poured into the reaction mixture. Citric acid was utilized as a chelating agent to ensure the uniform distribution of metal ions, thereby preventing phase separation during thermal treatment and facilitating the formation of porous structures during calcination, which enhanced the surface properties of the composites. After further stirring for 30 min, the addition of 1 M (150 mL) NaOH was carried out to adjust the pH of the solution to 5. Then, after further stirring for 1 h, the subsequent bluish-green precipitates were washed three times with DI water via centrifugation (4000 rpm) for 20 min to remove impurities. Next, dry at 70 °C for 16 h in an oven and calcined for 2 h at 400 °C in an electric furnace to obtain the CuO-NiO powder. [24]
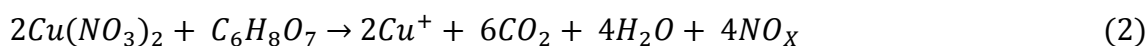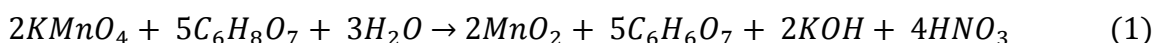
The PLN/CuO-NiO was synthesized via an *in-situ* polymerization technique using ferric chloride hexahydrate as a polymerizing agent. Ferric chloride hexahydrate ($FeCl_3·6H_2O$) as a polymerizing agent starts the oxidative polymerization of indole monomers, resulting in the formation of PLN chains on the surface of the composite. After being thoroughly washed, most iron species are eliminated, but elemental analysis shows that there is small amount of Fe residual that is strongly bonded to the polymer matrix are still remains in the final composites, reflecting its involvement in the synthesis process. Typically, in 50 mL of 1 N HCl solution, 1.3 g $FeCl_3.6H_2O$ was dissolved and stirred for 30 min by a magnetic stirrer. Meanwhile, 0.2 g CuO-NiO was spread in 20 mL DI water and sonicated for 15 min. Then, the solution was transported into the reaction mixture and further stirred for 30 min. Then, 2 g of indole solution in 30 mL of ethanol was prepared and added dropwise into the reaction mixture with magnetic stirring for 24 h to start the polymerization process. Consequently, the resulting mixture was washed away with

methanol and DI water via centrifugation (4000 rpm) for 20 min. Finally, dry the final product at 70 ˚C for 24 h to obtain a fine powder (Fig. 2). [30]

2.3 Synthesis of PLN/Mn-Cu

A hydrothermal approach was employed to prepare Mn-Cu. In the reaction procedure, 0.3 M (40 mL) $KMnO_4$ and 0.5 M (40 mL) copper nitrate trihydrate solution were prepared in DI water under magnetic stirring for 20 min. Then, 0.1 M (40 mL) citric acid monohydrate was poured into the reaction mixture through magnetic stirring for 3 h. Afterwards, the mixture was transferred to a Teflon-lined stainless-steel autoclave (150 mL) and heated at 150 ˚C for 12 h. To ensure uniform metal ion distribution and to facilitate the formation of porous structures, citric acid monohydrate was added as a mild reducing agent and chelating agent. When heated in water under hydrothermal conditions, Citric acid changes $KMnO_4$ (Mn^{7+}) to MnO_2 and Cu^{2+} ions to Cu^+ or CuO, allowing for the synthesis of mixed metal oxides with controlled valence states and preventing phase separation. The simplified reactions can be represented as follows:

$$2KMnO_4 + 5C_6H_8O_7 + 3H_2O \rightarrow 2MnO_2 + 5C_6H_6O_7 + 2KOH + 4HNO_3 \qquad (1)$$

$$2Cu(NO_3)_2 + C_6H_8O_7 \rightarrow 2Cu^+ + 6CO_2 + 4H_2O + 4NO_X \qquad (2)$$

Then, precipitates are washed with DI water to remove impurities and dried at 70 ˚C for 11 h.[31] For the preparation of PLN/Mn-Cu, an in-situ polymerization technique was used. Typically, 1.4 g $FeCl_3.6H_2O$ was added to a 1 N HCl (50 mL) solution under magnetic stirring for 30 min. After that, 0.1 g Mn-Cu was dispersed in 20 mL DI water and sonicated for 20 min. Meanwhile, the solution was poured into the above reaction mixture and further stirred for 30 min to obtain a homogeneous dispersion. Next, 2 g indole solution in 30 mL ethanol was prepared and poured dropwise into the above mixture via magnetic stirring for 24 h. Subsequently, the obtained precipitates were washed with methanol, and DI water via centrifugation (5000 rpm, for 20 min), and dried at 80 ˚C to obtain a final product (Fig. 3 and 4). [32]
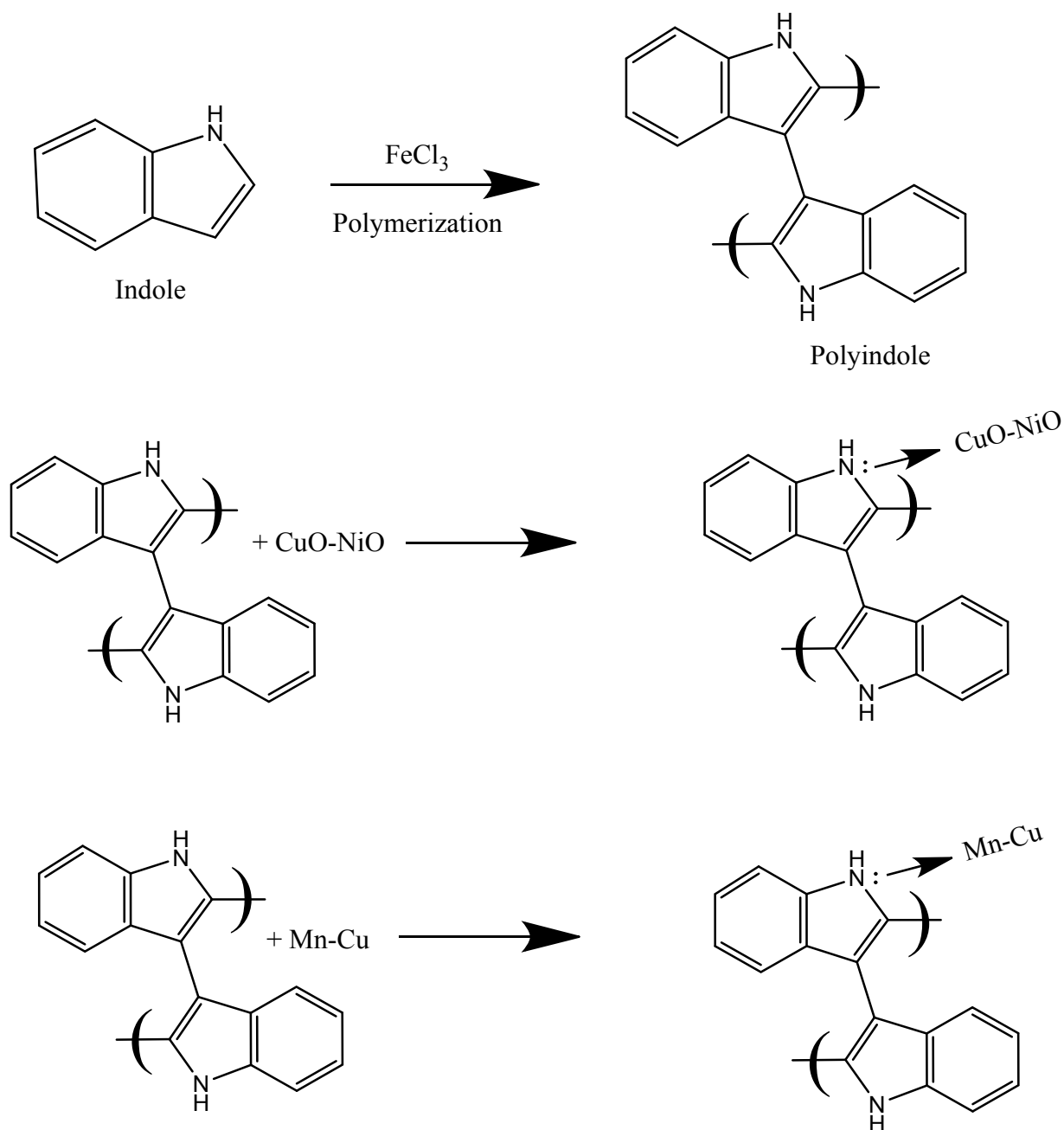
Fig. 2. Graphical diagram for preparation of **(A)** PLN/CuO-NiO and **(B)** PLN/Mn-Cu

Fig. 3. Structural representation of interaction mechanisms of PLN, PLN/CuO-NiO, and PLN/Mn-Cu

2.4 Characterization

The surface study of the test samples was analyzed with scanning electron microscopy (FEI Nova Nano Sem) operated at 20 KV, connected to an EDX acquisition detector used to determine elemental composition. [33] The ultraviolet-visible absorption spectra of composites were recorded

in the 250-900 nm range via a CE 7200 spectrophotometer, UK. [34] Functional group analysis of test specimens was carried out via extracted FTIR spectra in the 4000-650 cm^{-1} range using an Agilent (USA) Cary 360 Spectrophotometer. [35] The crystalline properties of the composites were obtained by a BRUKER D8 Model Powder Diffractometer (XRD) (USA) with (λ = 1.54 Å) at a scan range of 2θ=10–80°, working at 30 mA, and 40 kV. [36] From the XRD analysis, the average crystallite size of the prepared samples was calculated through Debye–Scherrer's formula.

$$D = \frac{K\lambda}{\beta COS\theta} \qquad (3)$$

Where K = shape factor, λ = 1.5406 Å, $\boldsymbol{\theta}$ = Bragg's angle, and β = line broadening at half maximum intensity.

2.5 Photocatalytic procedure

The synthesized PLN/CuO-NiO and PLN/Mn-Cu were tested against IMI pesticides to determine their photocatalytic activity. To examine the photocatalytic process, reaction parameters were set as 2–12 pH, 5–30 mg/L catalyst dose, 2-12 mg/L initial dye concentration, and 10–160 min contact time. The experiments were performed as follows: 0.01 g of the weighed composition of catalysts was poured into 100 mL of a 10-mg/L solution of imidacloprid pesticide with the addition of 10 mM of H_2O_2 as an oxidizing agent, and before irradiation to sunlight, the solution was first placed under dark light for 20 min to attain adsorption-desorption equilibrium. Then, a solution was put under direct exposure to visible light under shaking, working at 120 rpm. Afterwards, a definite time pause, 5 mL of test samples were taken from the reaction mixture and centrifuged at 4000 rpm for 15 min. The variation in IMI pesticide amount as a function of radiation time was examined using by UV/vis spectrophotometer by measuring the absorbance at λ_{max} of 270 nm. The IMI removal efficiency was calculated using equation (2).

$$Degradation\ (\%) = \left(\frac{A_0 - A_t}{A_0}\right) \times 100 \qquad (4)$$

Where "Ao" and "At" indicate initial (t=0 min) and equilibrium (t = t minutes) concentrations (mg/L) of pesticide, respectively.

3. Results and discussion

3.1 FTIR analysis

FTIR study was used to identify the presence of functional groups on the external surface of materials. The FTIR spectra of PLN, PLN/CuO-NiO and PLN/Mn-Cu were recorded in the range of 4000-650 cm^{-1} and responses thus assessed are displayed in Fig. 4. The intense IR band located at 3390 cm^{-1} is the characteristics NH stretching vibrational bond of PLN and the bond at 1561 cm^{-1} attributed to deformational vibration mode of NH bond and vibrational mode of C=C bonds aromatic ring of indole, respectively as depicted in Fig. 4A. These studies specify the existence of NH bond in the polyindole ring and indicates that the nitrogen atom of indole is not involved in the polymerization process. [37] The peaks positioned at 1448 and 1328 cm^{-1} represent C-N and C=N stretching modes of vibration of indole, respectively. The band positioned at 1094 cm^{-1} has been assigned to in-plane CH bonding modes existing in the aromatic heterocyclic part of indole. The sharp band at 733 cm^{-1} corresponds to the CH bond out of plane distortion, and the peak around 720 cm^{-1} shows in-phase vibrational movement of hydrogen atoms of 2 and 3 carbon site is missing. [38] These indications imply that the polymerization process does not occur at the benzene ring, and the 2, 3 position of pyrrole is responsible for the polymerization process.

The existence of a broad peak around 3400 cm^{-1} is ascribed to the OH stretching vibration of water molecules in the sample of CuO-NiO, as shown in Fig. 4B. The peak appeared near 1600 cm^{-1} due to the bending vibration of water adsorbed on the surface. The presence of a peak around 2300 cm^{-1} is indicative of the existence of CO_2 in the samples. Hence, a peak at 1127 cm^{-1} assigned to Cu-O-Ni interactions, confirmed the formation of nanoparticles. Furthermore, the two peaks identified at 1461 and 860 cm^{-1} corresponded to the metal oxide vibration mode in the sample. [39] Hence, FTIR spectrum confirms the PLN/ CuO-NiO has characteristic absorption bands at 3410, 2282, 1548, 1450, 1328, and 740 cm^{-1} for OH, CO_2, aromatic C=C, C-N, C=N, and C-H out of plane in benzene, respectively. [40] The results show that peaks of polymer are blue-shifted, which indicates that a covalent bond is formed between polymer and composite in the formation of PLN/ CuO-NiO.

An intense peak at 3400 cm^{-1} is due to OH of absorbed water, and a peak around 3600 cm^{-1} revealed Mn-OH vibration in the structure of Mn-Cu and PLN/ Mn-Cu, respectively (Fig. 4C). A sharp band at 747 cm^{-1} is due to Mn-Cu-O, and at 1067 cm^{-1} is ascribed to the stretching mode of C-O in Mn-Cu. [41] A bifurcated peak around 1600 cm^{-1} arose due to the absorption of atmospheric CO_2 on the surface of nanoparticles. The bands that appeared at 1075 and 735 cm^{-1} are indicative of the C-H stretching mode of vibration in the structure of the benzene ring
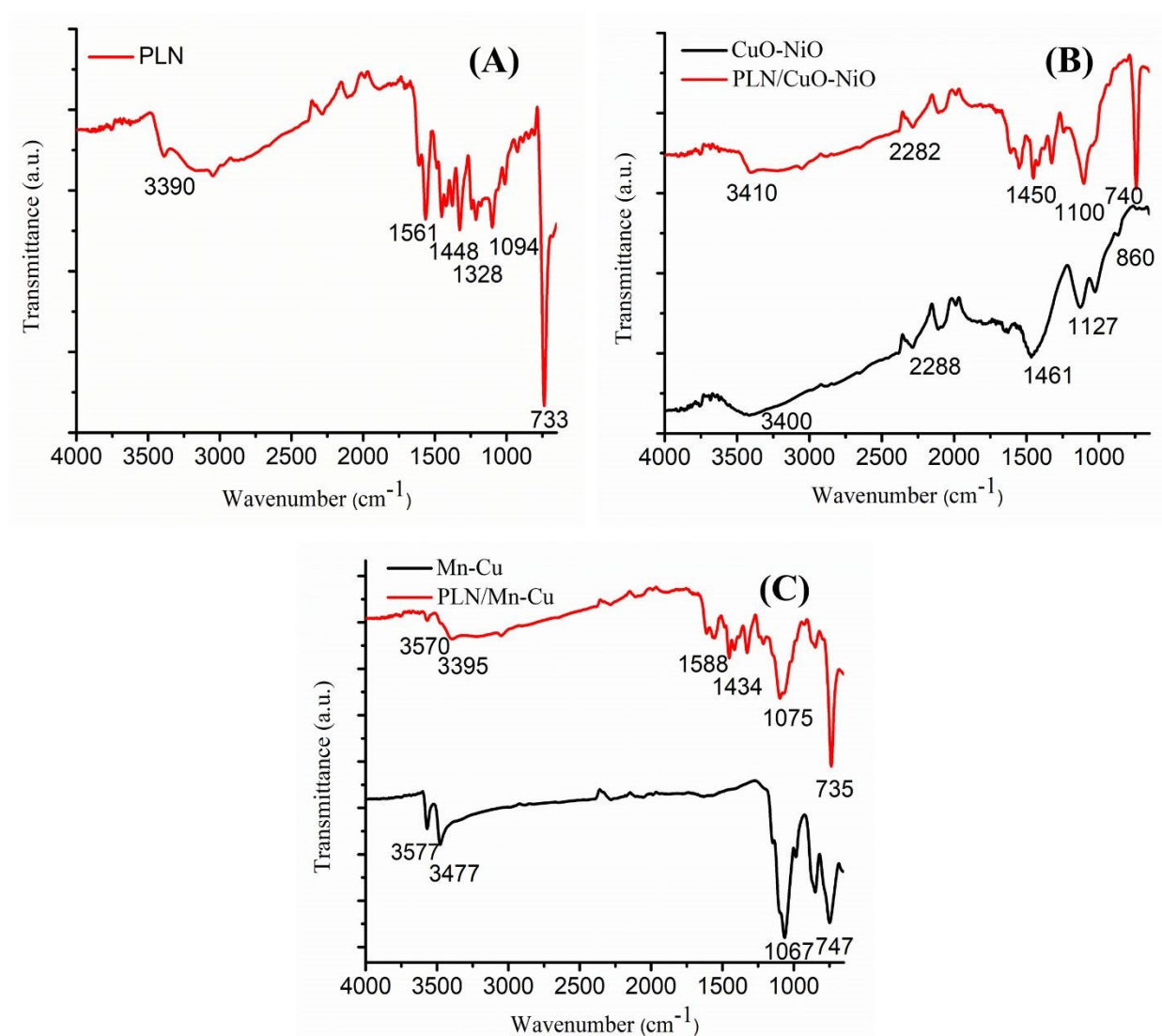

Fig. 4. FTIR spectra of (**A**) PLN, (**B**) CuO-NiO, PLN/CuO-NiO, and (**C**) Mn-Cu, PLN/Mn-Cu

[42]. A slight shift in the wavenumber values in the spectrum of PLN/ Mn- Cu revealed the interaction between polymer and composite material and validated the formation of PBNC.

3.2 Optical analysis

UV-vis spectroscopy helps to evaluate the absorbance, transmittance, and inner transition in the particles and their band gap study. [43] The UV-Vis absorption spectra of the synthesized composites were recorded in the range of 250-900 nm, as shown in Fig. 5. A strong absorption band of CuO-NiO was obtained at 250 nm in the ultraviolet region (Fig. 6A). The absorption rate of the composite decreased drastically to a blue shift due to the formation of CuO-NiO composite. The deposition of PLN into the composite results in a redshift of PLN/CuO-NiO at 304 nm. [44] The UV spectral peaks of Mn-Cu and PLN/Mn-Cu were evaluated at wavelength values 275 and 280 nm, respectively (Fig. 5B). The sharpness and intensity of UV-vis spectra indicate that the synthesized composites are nanosized. [45]

The difference in excitation energy from the valence band to the conduction band in a material under study is known as the band gap energy (E_g). [46] The photocatalytic efficiency of a composite depended upon its E_g value, which was determined from the well-known Tauc's plot relation.

$$\alpha h v = Z(hv - Eg)^n \tag{6}$$

Z is the band tailing parameter, hv is the energy of a photon, Eg Is the calculation for the nanoparticle band gap, and α is the absorption coefficient calculated by

$$\alpha = 2.303 \frac{A}{d} \tag{7}$$

Here, A is the absorbance and d is considered as sample thickness or cuvette path length, by plotting graphs between $(\alpha hv)^2$ and the hv. Eg The value of the composites under consideration was calculated. [47] The photocatalysts having E_g values greater than 3 would absorb efficiently into the visible region and vice versa. From the Tauc plot, the values of the direct optical band gap were determined to be 2.38 eV for CuO-NiO, 2.13 eV for PLN/CuO-NiO (Fig. 5C), 2.34 eV for Mn-Cu, and 2.15 eV for PLN/Mn-Cu (Fig. 5D), respectively. [48] The optical bandgap value decreases with the addition of polymer into the composites, because of the generation of electrons that reduces the band gap.
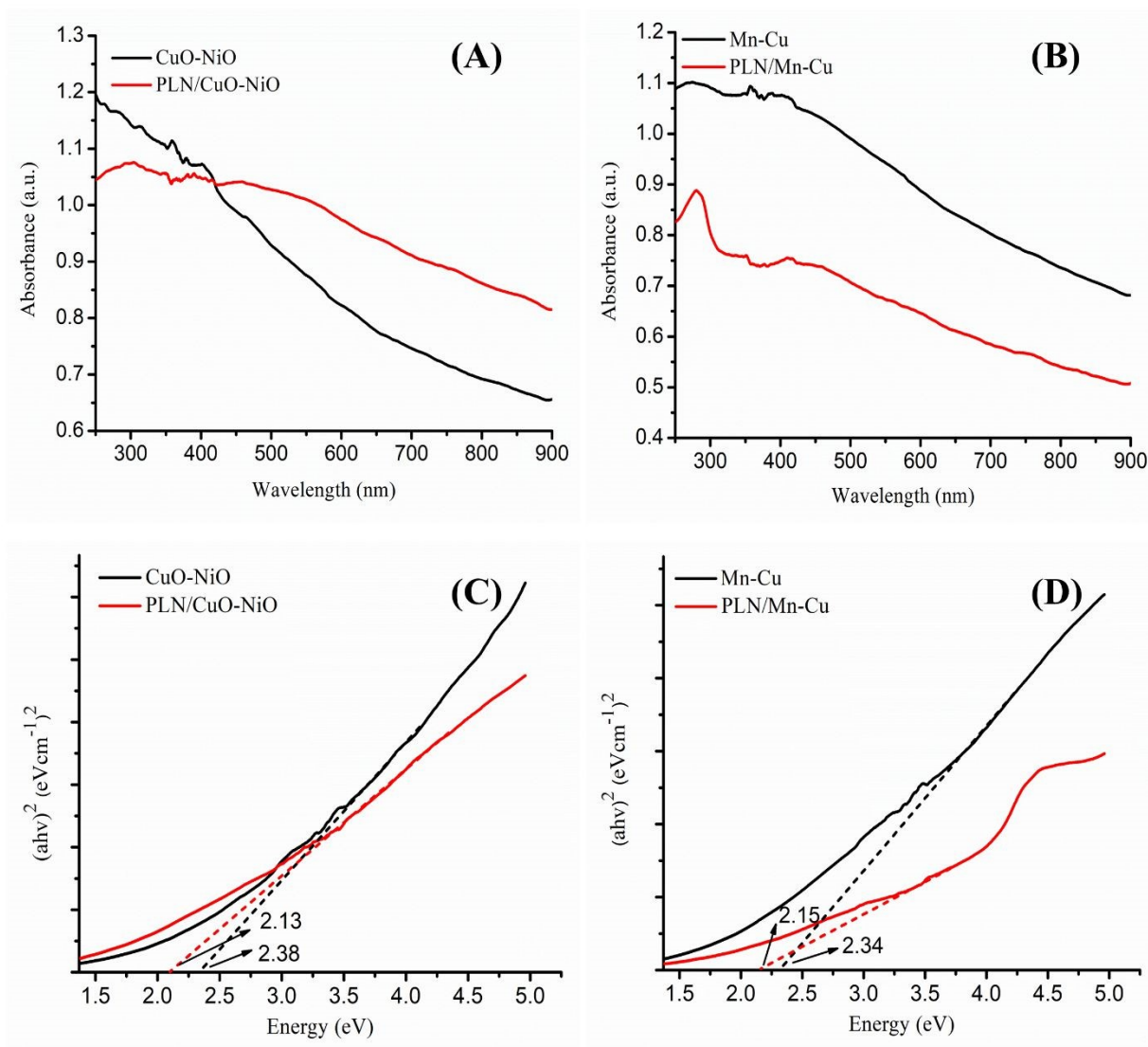
Fig. 5 (A) and **(B)** show UV-visible spectra, and **(C)** and **(D)** show Tauc's plots for the energy band gap of Mn-Cu, PLN/Mn-Cu, and CuO-NiO, PLN/CuO-NiO, respectively

3. 3 Surface morphology

The surface morphology study of nanocomposites was examined with SEM analysis. The magnified images of the samples were taken at a 5 µm scale. [49] SEM images and histogram of PLN/CuO-NiO and PLN/Mn-Cu are depicted in Fig. 6. The image reveals that PLN/CuO-NiO composite displays predominantly spherical particles with some irregularities at the edges, indicating partial agglomeration (Fig. 6A). The Mn-Cu composite exhibits a granular morphology is composed of small, irregularly shaped particles forming loosely packed clusters, giving a

heterogeneous surface appearance, and there is a presence of PLN sheets in the sample (Fig. 6B). The slight presence of agglomeration is attributed to surface tension and high surface energy of the composites. [50] Meanwhile, Mn-Cu and CuO-NiO are uniformly distributed and cover the surface of PLN sheets, which confirms the existence of these nanoparticles on PLN sheets. From SEM images, it is shown that the incorporation of PLN on these nanocomposites provides enough surface area for electron transfer and increased reaction sites [37]. The SEM images of the composites were further examined by ImageJ software to determine their average particle size distribution. The average size distribution of the PLN/CuO-NiO is found to be 75 nm, through 120 measurements as depicted in Fig. 6C. While from a total of 100 measurements taken, the average size for PLN/Mn-Cu was calculated to be 118 nm Fig. 6D. Furthermore, this calculated size was higher than the average size determined from the Debye-Scherrer formula. [51] This difference is due to the effect of lattice strain on crystal structure, which is not measured Debye-Scherrer equation.
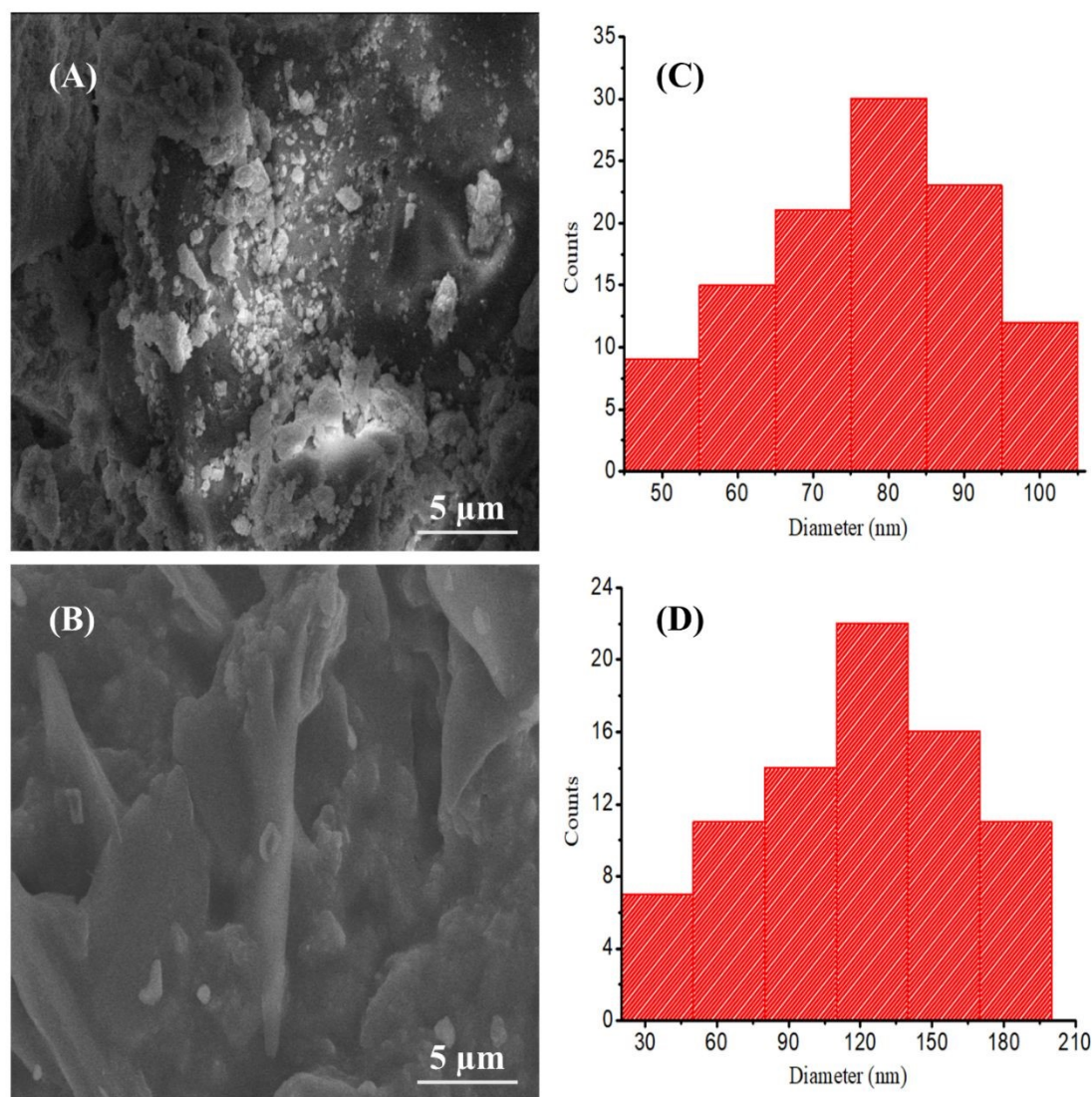
Materials Advances Accepted Manuscript

Fig. 6. SEM micrographs of **(A)** PLN/CuO-NiO, **(B)** PLN/Mn-Cu with corresponding histogram **(C)** PLN/CuO-NiO and **(D)** PLN/Mn-Cu

3. 4 XRD analysis

The XRD technique was used to examine the crystallinity and phase purity of prepared composites and the XRD pattern of materials is depicted in Fig. 8. In the XRD pattern of PLN/Mn-Cu, the 2θ angles of 17.3°, 28.9°, 35.4°, 39.2°, 41.8°, 46.4°, 47.9°, 53.8° 56.7°, 68.5° were assigned to the (111), (200), (220), (311), (222), (400), (331), (422), (333), (315) lattice planes, attributed to the face centered cubic structure of Mn_3O_4 (JCPDS No. 24-0734) and metallic Cu (JCPDS No. 04-0836) phases in the composite with the presence of sharp intense peaks showing a good

crystallinity in the material as shown in Fig. 7. [55] Furthermore, there are a few low-intensity diffraction peaks obtained at 2θ values 19.2°, 24.2°, and 26.8°, which indicate the presence of PLN in PLN/Mn-Cu with an amorphous nature. The values of lattice parameters of the test specimen were obtained as a = 4.710 (Å), b = 4.710 (Å), and c = 4.710 (Å). The planes patterns (011), (1 11), (110), (020), (121), (022), (1 32) at 2θ values of 13.3°, 16.7°, 22.7°, 28.9°, 44.4°, 52.6°, 60.1°, 65.91°, respectively, correspond to PLN/CuO-NiO match well with monoclinic CuO (JCPDS No. 45-0937) and cubic structure of NiO (JCPDS No. 47-1049) [56] with values of lattice parameters observed in the composite are a = 4.2520 (Å), b = 4.2520 (Å), and c = 4.2520 (Å). The presence of intense peaks at 19.6° and 25.5° confirms the presence of PLN with a partial crystalline nature [57]. It concluded that the existence of PLN peaks confirms its incorporation into the CuO-NiO composite. The sharp intensity peaks centered below 20° values demonstrate crystallinity in the composite material. The average crystal size of the composites was calculated using the Debye-Scherrer formula, based on the highest intensity peaks, that is (200) at 28.9° and (111) at 16.7° of the prepared PBNCs, respectively. The average crystal size was found to be 79 and 54 nm for PLN/Mn-Cu and PLN/CuO-NiO, respectively. The obtained results of lattice parameters and volumes of unit cells are illustrated in Table 1.
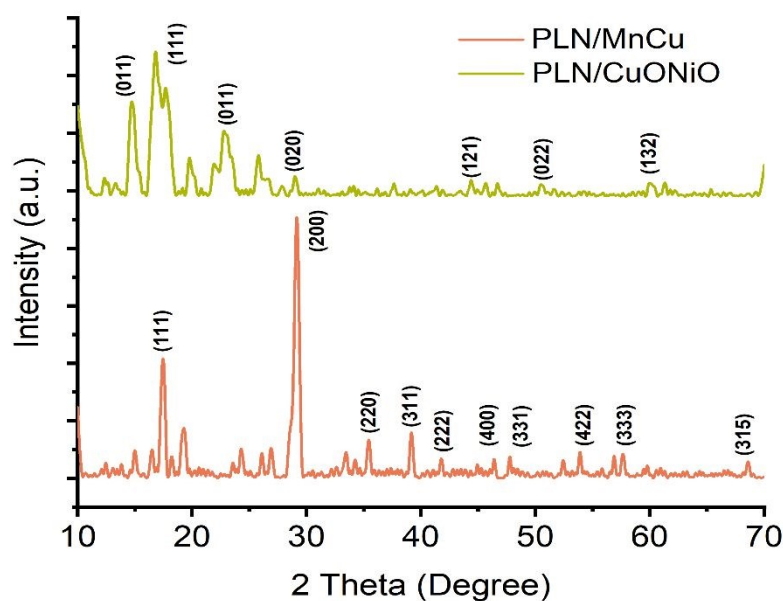

Fig. 7. XRD pattern of PLN/Mn-Cu and PLN/CuO-NiO PBNCs

Table 1. XRD data peaks for PLN/Mn-Cu and PLN/CuO-NiO

Phase	Lattice constants (Å)	Unit cell volume (Å³)
Face centered-cubic (PLN/Mn-Cu)	a = 4.710 b = 4.710 c = 4.710	104.49
Cubic (PLN/CuO-NiO)	a = 4.2520 b = 4.2520 c = 4.2520	76.87

3. 5 Photocatalytic performances

3. 5.1 Effect of pH and point of zero charge (PZC) analysis

The surface catalytic properties of the BNCs and treated PLN could be explained in terms of the point of PZC, the point at which the charge on the surface of the catalyst becomes zero. [58] If the pH_{PZC} is higher than the optimized pH of the composite, the composite surface will have a positive charge, and if the pH_{PZC} is lower than the optimum pH, the composite surface will possess a negative charge. The catalyst surface charge helps determine out anions and cations degradation capability. [59] Sodium chloride (NaCl) (0.1 M) solution was used to determine pHpzc, and the results are depicted in Fig. 8A. The pHpzc was calculated to be 6.28 and 6.48 in the case of PLN/CuO-NiO and PLN/Mn-Cu, respectively [60]. The pH is the dominant parameter in the degradation procedure. By varying the pH, the interaction between composites and imidacloprid was altered, which was studied in the range of 2-12 pH.

Imidacloprid is present in its neutral form, but its degradation is facilitated by reaction conditions, which can be accelerated in more acidic and alkaline environments. [61] The result indicated that maximum degradation capacities of 91 and 98 (%) were achieved for the PBNCs at pH 4 and 10, respectively (Fig. 8B). It was observed that acidic pH was reliable for degradation via PLN/CuO-NiO under irradiation, which is due to the reason that in acidic pH due to higher

Materials Advances Accepted Manuscript

concentration of H^+, the electrostatic attractions between positive charge composite surface and negatively charged pesticide molecules increases and consequently, degradation capacity was enhanced which could be explained using pHpzc concept. [62] Under alkaline conditions, the surface of a PLN/Mn-Cu changed to negatively charged at pH 10 due to the generation of hydroxyl radicals and supporting the photodegradation of cationic IMI molecules. [63] Hence, higher pH levels than 10 did not favor the degradation process because alkaline media block the active sites of composites and preclude them from efficient degradation.

3. 5.2. Effect of composite dose

The composite dosage has a significant influence on degradation; meanwhile, degradation depends upon the active sites present on the surface of the composite. The composite dosage effect was studied from 5 to 30 mg/L (Fig. 8C). The maximum degradation of IMI was obtained when a 5 mg/L dose of all composites was used. The degradation values at the optimum dose (5 mg/L) for PLN/CuO-NiO and PLN/Mn-Cu were 91 and 98 (%), respectively [64]. As the dosage amount was augmented from the optimum value, a decline in degradation efficiency of the nanoparticles occurred, owing to the agglomeration of composite particles, which cover the available active moieties, and also, less light penetration occurs. [65] Also, at higher doses, all the active moieties become saturated with the establishment of equilibrium, and at this point, pesticide molecules are released back to solution from the composite surface, and the removal efficiency declines. [66]

3. 5.3. Effect of contact time

Contact time is a crucial parameter and affects the percentage degradation of IMI under optimal conditions, which were studied from 5 to 150 min, and the output depicted in Fig. 8D. The Photocatalytic process necessitates the presence of O_2, H_2O, and light irradiation on the prepared composite surface to form electron-hole pairs. [67] At the start of the reaction, these bind to the surface of the composite due to a greater amount, and the rate of degradation was initially very fast, gradually slowed down, and finally reached the equilibrium values, which indicate the saturation point. Experimental studies show that the optimum time was 120 min for PLN/Mn-Cu and 60 min for PLN/CuO-NiO, having degradation capacities of 91 and 98 (%), respectively. As the reaction proceeds after the optimum time, all the available active sites become saturated, resultantly in the unavailability of active sites; already occupied binding sites repel the incoming pesticide molecules, and the rate of degradation becomes constant. [68]

3. 5.4. Effect of imidacloprid concentration

The IMI concentration affects the degradation pathway due to the gradient factor and mass transfer. The effect of IMI concentration was assessed in 2 to 12 mg/L, keeping other parameters constant (Fig. 8E). The sequestration efficiency was increased as the initial concentration increased up to 6 mg/L via PLN/CuO-NiO, and after that, it was decreased. [69] The optimum initial concentration point was 2 mg/L via PLN/Mn-Cu. It is due to the reason that at low pesticide initial concentration, the number of available active sites was high and the removal capacity was raised till the optimum point. [70] After that point, the diffusion of pesticide molecules to the composite surface becomes less efficient, which results in a reduction of the generation of reactive species necessary for degradation, such as hydroxyl radicals, reducing their availability for further concentration at higher concentrations. The IMI sequestration efficiency was recorded to be 84% and 87% using the given PBNCs, respectively.
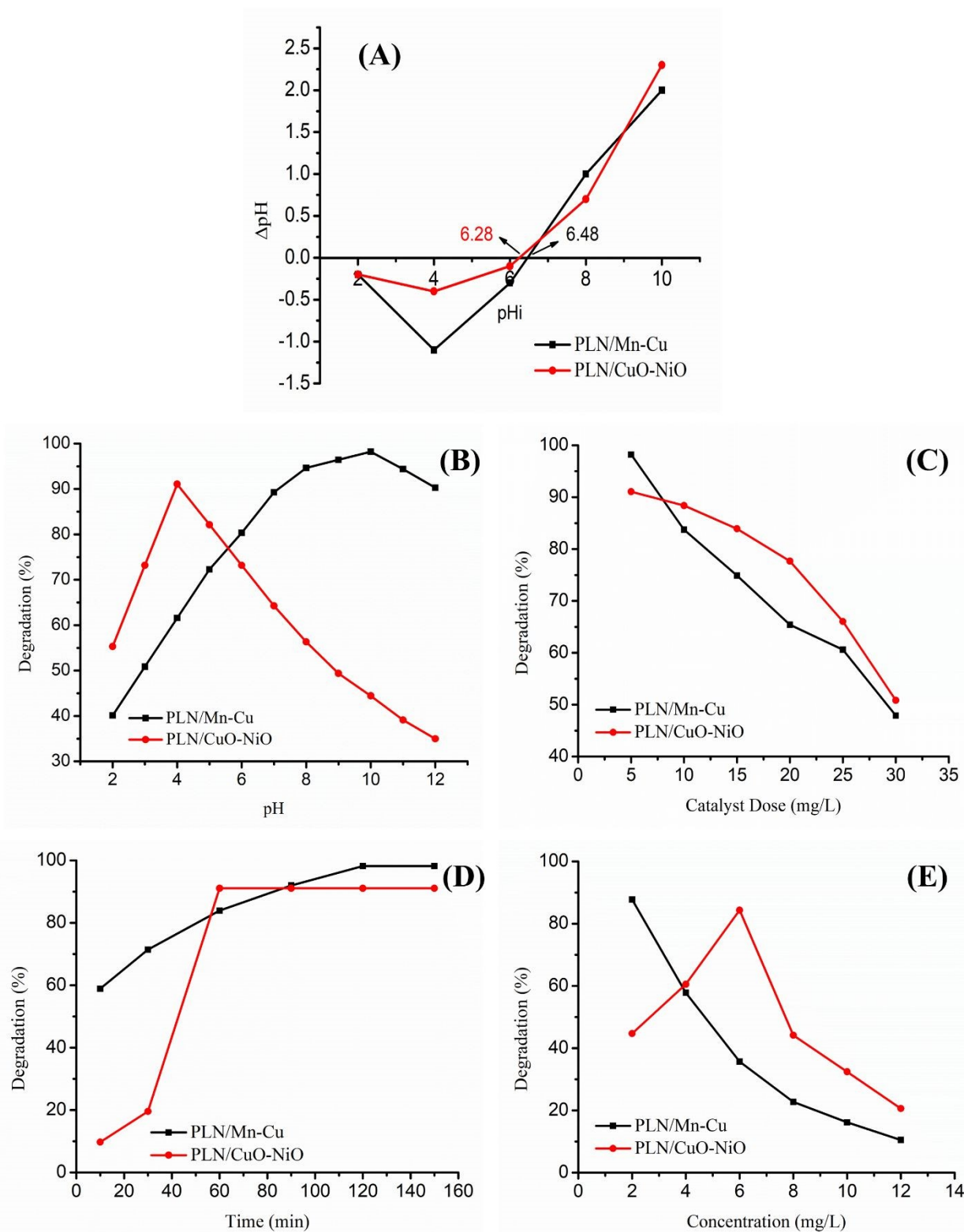
Fig. 8. (A) pH$_{PZC}$ measurement, **(B)** effect of pH, **(C)** effect of catalyst dose, **(D)** effect of irradiation time, and **(E)** effect of pesticide concentration on IMI photodegradation rate via

PLN/Mn-Cu and PLN/CuO-NiO

3. 6 Effect of oxidant dose

Hydrogen peroxide is an effective oxidant and its combination with ultraviolet light or composites for the remediation of wastewater, however, has been demonstrated to be an innovative technology. The photocatalytic removal of IMI was studied in the absence and presence of H_2O_2 (at various concentrations) and responses are shown in Fig. 9(A). [71] A blank experiment was performed in the absence of H_2O_2 to analyze the degradation efficiency of IMI by PLN/Mn-Cu and PLN/CuO-NiO, which were found to be 59 and 54%, respectively. The role of H_2O_2 is to act as an electron acceptor and thus capability to endorse charge separation and also yield OH^- through the following equation. [72]

$$H_2O_2 + e^- \rightarrow OH^\bullet + OH^\bullet \tag{7}$$

To elucidate the effect of oxidant, the concentration of H_2O_2 was varied over a range of 5 -20 mM. It has been observed that a significant improvement in the removal of IMI was demonstrated till the optimum amount of 10 mM. It is obvious that at a lower concentration of oxidant, the photogenerated electron and hole can recombine due to a suitable concentration of scavengers (hydroxyl radicals and holes) to degrade the pesticide. [73] After optimal concentration, there is a decline in the process. It is because, at a higher amount of oxidant, the hydroxyl radical formed is converted into hydroperoxyl radicals, causing to decrease in the penetration of UV light on the surface of the catalyst and the rate of removal. [74] The production of hydroperoxyl radicals occurs as presented in Eqs. 7-11 and Fig. 10.

$$OH^\bullet + OH^\bullet \rightarrow H_2O_2 \tag{8}$$

$$H_2O_2 + OH^\bullet \rightarrow OH_2^\bullet + H_2O \tag{9}$$

$$OH_2^\bullet + OH_2^\bullet \rightarrow H_2O_2 + O_2 \tag{10}$$

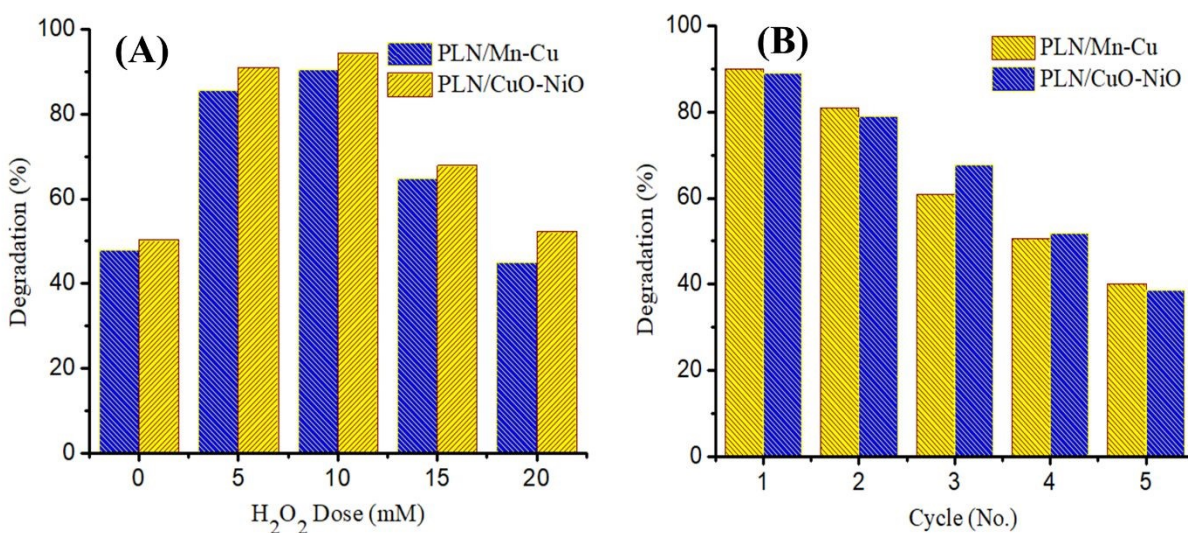$$OH^\bullet + O_2 \rightarrow OH_2^\bullet + O^\bullet \tag{11}$$

Fig. 9. (A) Effect of dosage on IMI removal via synthesized nanocomposites and (B) catalysts reusability and stability in five successive cycles for photodegradation of IMI

3. 7. Reusability of catalyst

The reusability and stability of PBNCs were economically important in removing pesticide pollutants from aqueous solution by applying the optimal experimental conditions. The prepared catalysts were isolated from the solution after the first test, then washed thoroughly with distilled water and allowed to dry. The catalyst stability was evaluated in five cycles with an IMI concentration of 10 mg/L (Fig. 9B). After five cycles, the removal efficiency of IMI decreased from 98 91% to 38% and 35% via PLN/Mn-Cu and PLN/CuO-NiO, respectively. [75] This decrease in the catalytic activity of photocatalysts could be attributed to the following reasons: (1) material loss occurs in water in the recovery step after every cycle, which leads to a decrease in degrading performance. [76] (2) aggregation of nanoparticles causes to reduction in binding sites and effective surface area necessary for pesticide molecules to attach. [77] (3) Obstruction of pores of active sites

due to the development of intermediate molecules on the catalyst surface gradually decreased the removal efficacy.
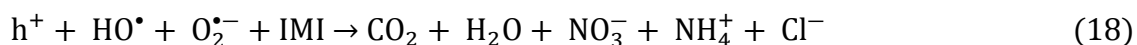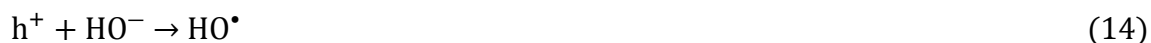
3. 8. Photocatalytic degradation mechanism

The charge transfer mechanism in the prepared nanocomposites under sunlight irradiation is shown in Fig 10. When PLN/CuO-NiO and PLN/Mn-Cu nanocomposites are exposed to visible light, they absorb photons, which causes electrons to move from the valence band (VB) to the conduction band (CB), leaving holes in the VB. These composites are effective photocatalysts for visible light due to their small band gaps, specifically 2.13 eV and 2.15 eV, respectively. The CB potential for PLN/CuO-NiO is about −0.62 eV, and the VB is +1.51 eV compared to NHE. Similarly, PLN/Mn-Cu has CB and VB values of −0.61 eV and +1.54 eV, respectively. The excited electrons (e^-) in CB break down surface adsorbed oxygen (O_2, $E° = -0.33$ eV) to generate superoxide radicals ($O_2•^-$). Subsequently, these radicals make hydrogen peroxide (H_2O_2) and then further hydroxyl radicals (•OH). At the same time, the holes (h^+) that are made by light in the VB oxidize (oxidation potential greater than +1.23 eV) water (H_2O) or hydroxide ions (OH^-), which produce further •OH radicals. These reactive oxygen species (ROS) are responsible for the degradation of imidacloprid [78].

The nitrogen-rich imidacloprid molecule is oxidatively cleaved by •OH and $O_2•^-$ attack, resulting in the formation of intermediate products like short-chain organic acids, urea-type fragments, and nitroso derivatives. These intermediates eventually mineralize into CO_2, H_2O, and nitrogen-containing species, such as NO_3^- and NH_4^+. [79] Additionally, the polyindole (PLN) coating increases the generation of reactive radicals and decreases electron-hole recombination by promoting improved charge separation and interfacial charge transfer. The existence of bimetallic CuO-NiO and Mn-Cu heterojunctions further supports efficient charge migration pathways. This may occur through either a Z-scheme mechanism, which separates electrons and holes while maintaining their potent redox ability, or a Type II heterojunction. [80] The charge carrier dynamics mechanism in PLN/Composites during the photocatalytic degradation process is demonstrated by the reactions shown in Eqs. 12-18.

The pesticide solutions were examined under FTIR to track the metabolites and successfulness of the photodegradation process (Fig. 11). [85] The pristine IMI expressed peaks at

3310 cm-1 due to the N-H stretching of the imidazolidine ring which is masked by O-H peak arising due to the presence of moisture. The peaks at 1529, 1415 and 1222 cm-1 attributes the NO_2 stretching, C=C stretching and C=N stretching in the pyridine ring (Fig. 11a). The FTIR spectrum of aqueous solution of IMI expressed a sharp peak at 3305 cm-1, which is the characteristic peak of O-H stretching in water molecule (Fig.13b). On complete degradation of the IMI molecules, most of the peaks disappeared while some peaks at 3293 and 1637 cm-1 for H-O-H stretching vibrations due to aqueous media (Fig. 11c). [86] Based on the comparative data in Table 2, the present study demonstrates several advantages over previously reported photocatalysts. While earlier systems such as PPY/CuO–NiO and Ni@$ZnO_{0.6}S_{0.4}$/SPID required longer irradiation times (180–300 min) to achieve moderate to high degradation efficiencies (83–90%), and ZnO/$CoFe_2O_4$ achieved rapid degradation (98% in 45 min) but at a higher catalyst dose, the PLN/Mn–Cu and PLN/CuO–NiO catalysts in this work achieved high degradation of Imidacloprid (91–98%) under visible light with comparatively lower irradiation times (60–120 min). These results highlight the advantage of the present investigation in terms of efficient visible-light activity, shorter degradation times, and high pollutant removal rates, establishing the proposed PLN-based composites as highly effective and sustainable photocatalysts compared to previously reported systems.

$$PLN/Composites + h\nu \rightarrow e^- + h^+ \qquad (12)$$

$$h^+ + H_2O \rightarrow HO^\bullet + H^+ \qquad (13)$$

$$h^+ + HO^- \rightarrow HO^\bullet \qquad (14)$$

$$e^- + O_2 \rightarrow O_2^{\bullet-} \qquad (15) \quad O_2^{\bullet-} +$$

$$e^- + 2H^+ \rightarrow H_2O_2 \qquad (16)$$

$$H_2O_2 \rightarrow 2HO^\bullet \qquad (17)$$

$$h^+ + HO^\bullet + O_2^{\bullet-} + IMI \rightarrow CO_2 + H_2O + NO_3^- + NH_4^+ + Cl^- \qquad (18)$$
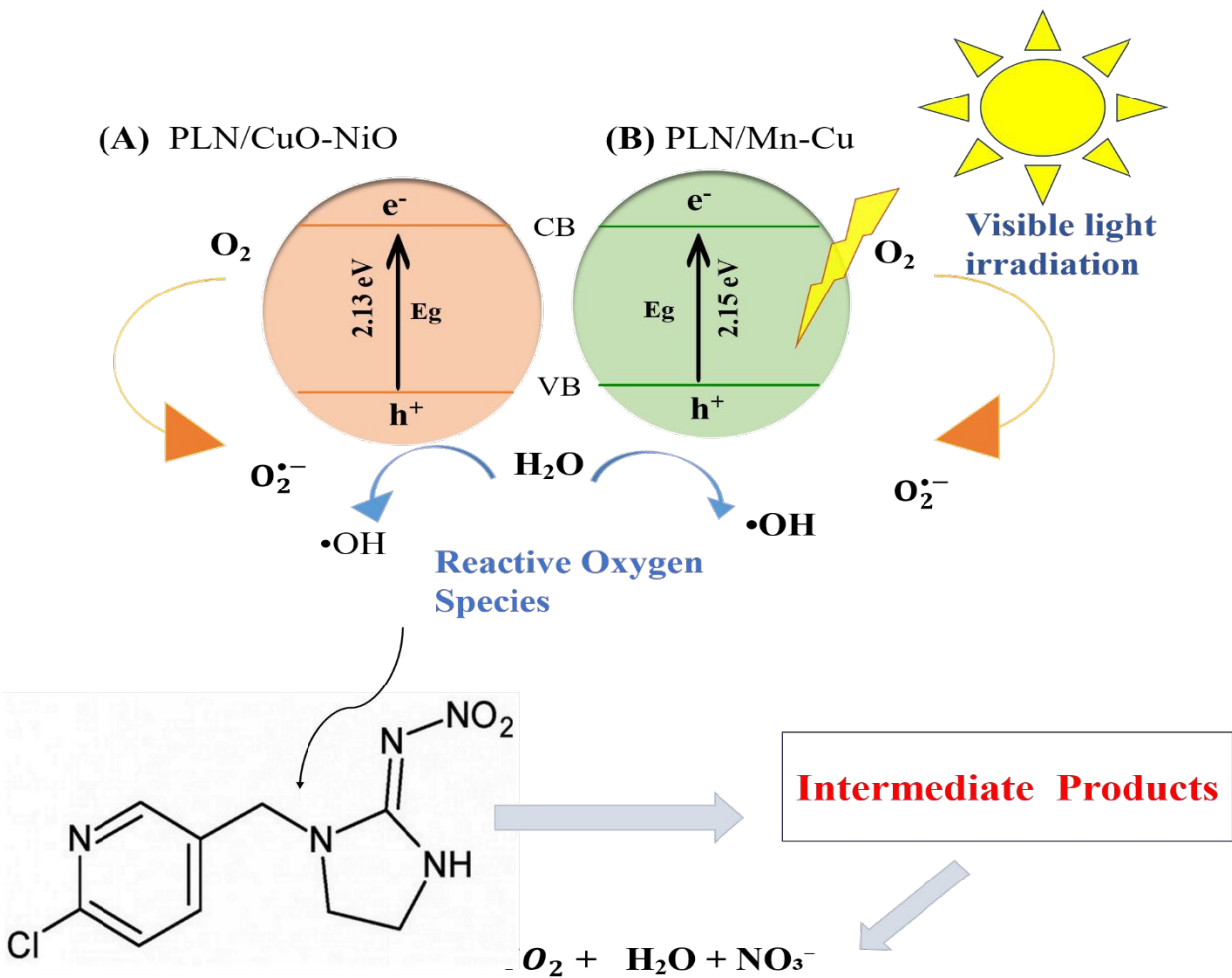
Fig. 10. Schematic illustration of the photocatalytic degradation mechanism of Imidacloprid

Table 2. Comparison of the photocatalytic activity of PLN/Mn-Cu and PLN/CuO-NiO with various photocatalysts

| Photocatalyst	Pollutant	Catalyst dose (g/L)	Light source	Time (min)	Degradation (%)	References
PPY/CuO-NiO	Alizarin Red	0.1	Uv	300	86	[24]
PPY/CuO-ZnO	Metanil Yellow	0.1	Vis	180	90	[81]
Gr-PLN	2,4-D	0.015	Uv	120	99	[30]
Ni@ZnO0.6S0.4/SPID	Bisphenol A	1	Vis	180	83	[82]
Mn-Cu$_2$O	Amoxicillin	1	Vis	180	92	[83]
ZnO/CoFe2O4	Imidacloprid	0.05	Vis	45	98	[84]
PLN/Mn-Cu	Imidacloprid		Vis	120	98	This work
PLN/CuO-NiO	Imidacloprid		Vis	60	91	This work
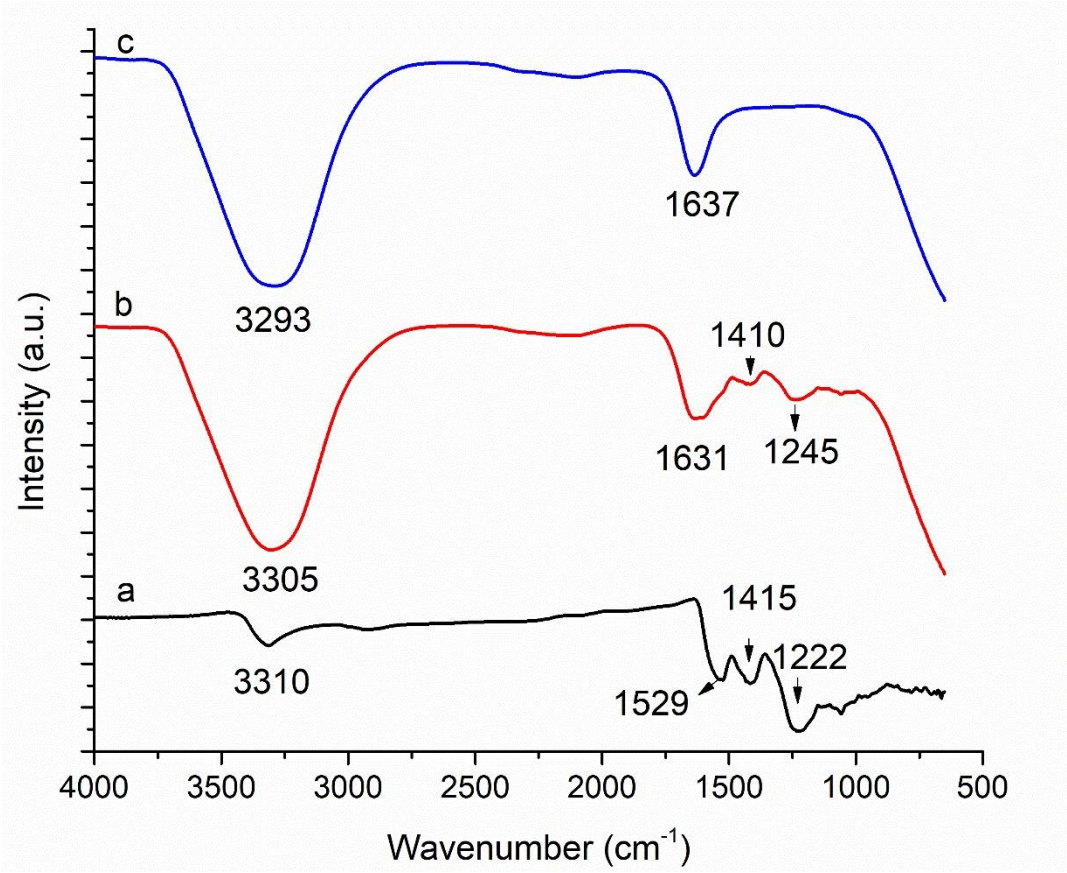
Fig. 11. FTIR spectra of (a) pristine IMI, (b) aqueous solution of IMI and (c) aqueous solution of IMI after degradation

3. 10. Kinetic analyses

The algorithm designed for pseudo first (PFO), pseudo second order (PSO) and Behnajady-Modirshala-Ghanbery (BMG) kinetic models was employed on IMI sequestration data to determine the coefficient of determination (R^2) and their corresponding kinetic variables values (Fig. 12). [87] The order of reaction was estimated via the degree of fit, which was evaluated by the value of R^2, which is the approach to 1, indicating the whole alignment between the experimental data and the data obtained from kinetic models. [88] Through optimization of kinetic models, the rate constant of the reaction was determined via a linear regression equation. Commonly, the removal of organic pollutants from wastewater through advanced oxidation processes (AOPs) can be described by eq. (19)

$$-\frac{dC}{dt} = K1C^n \qquad (19)$$

Here, C indicates pollutant concentration, k1 = rate constant, t = time, and n = order of reaction and its value is 1 for a first-order reaction. [89] After integration, eq. (19) Becomes as eq. (20)

$$C_t = C_o e^{-kt} \qquad (20)$$

Taking natural logs on both sides

$$ln[C_t] = ln[C_o] - k1t \qquad (21)$$

Eq. (12) can be written as,

$$ln\left(\frac{C_o}{C_t}\right) = k1t \qquad (22)$$

This is the linear equation representing the PFO model. Here Co and C_t Indicate IMI concentration at time t = 0 and concentration at t = t, k1 is the rate constant and t is the reaction time, respectively. The plot of $ln\left(\frac{C_o}{C_t}\right)$ vs time gives the value of slope equal to PFO rate constant (k1). The R^2 values obtained after applying the PFO kinetic model were 0.919, and 0.675 for PLN/Mn-Cu and PLN/CuO-NiO, respectively, showing that the PFO kinetic model was not fitted to the experimental data [90]. For second-order reactions, the value of n is 2.

$$-\frac{dC}{dt} = K_2C^2 \qquad (23)$$

Hence, after integration and rearranging the equation. (23) changes to eq. (24)

$$\frac{1}{C_t} = \frac{1}{C_0} + K_2 t \qquad\qquad (24)$$

The plot between time and $1/C_t$ Shows Fig.12 that the R^2 values of the PSO kinetic model were 0.889 and 0.674 for PLN/Mn-Cu and PLN/CuO-NiO, respectively. These values showed that the model was not suitable to describe the removal of pesticides. [91]

The kinetics of IMI pesticide can also be studied using the BMG model and defined in Eq. (25)

$$\frac{t}{1 - \frac{C_o}{C_t}} = m + bt \qquad\qquad (25)$$

The plot of factor t/1−Ct/Co versus time shows a straight line having an intercept value of m and a slope gives the value b. kinetic data obtained from the BMG model indicated that R^2 values were 0.915 and 0.998 for PLN/Mn-Cu and PLN/CuO-NiO, respectively (Fig. 12). Hence, BMG kinetic model shows high compatibility with the experimental data as associated with other kinetic models to describe the removal kinetics of IMI pesticide and fitted best model. [92] The rate constants and R^2 values for IMI degradation via the photocatalytic process under optimized conditions are reported in Table 3.
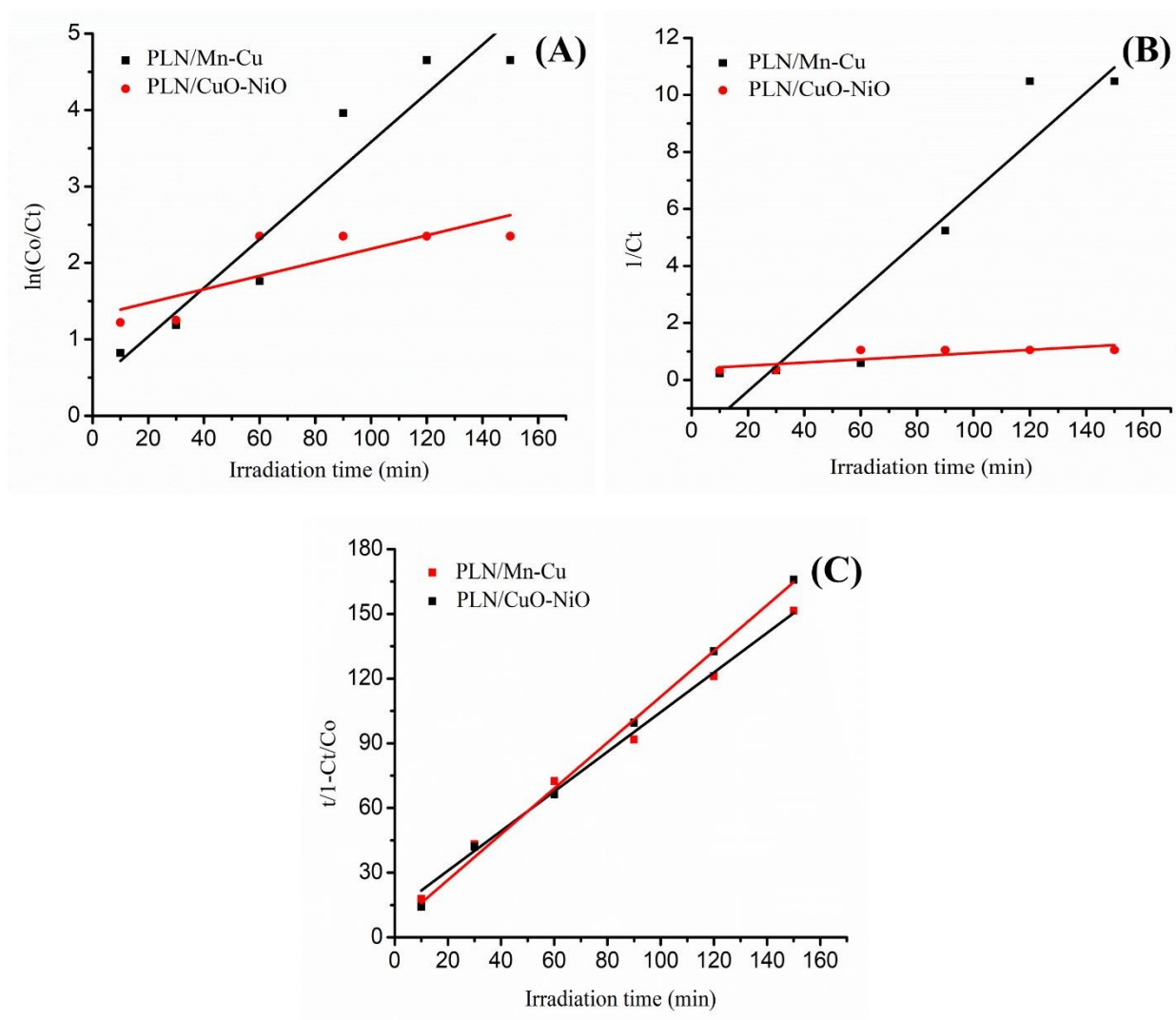
Fig. 12. Kinetic study **(A)** pseudo first order, **(B)** pseudo second order and **(D)** BMG kinetic modelling on photodegradation of IMI using PLN/Mn-Cu and PLN/CuO-NiO

Table 3. Kinetics variables for the removal of IMI using synthesized composites

Kinetic parameters	PLN/Mn-Cu	PLN/CuO-NiO
Pseudo-first order		
K_1 (min^{-1})	0.032	0.001
R^2	0.919	0.675
Pseudo-second order		
K_2 (min^{-1})	0.087	0.006
R^2	0.889	0.674
BMG kinetic model		
m (min)	12.528	5.326
b	0.919	1.062
R^2	0.995	0.998

4. Conclusion

In this study, for the first time PLN/Mn-Cu and PLN/CuO-NiO, bimetallic nanocomposites of transition metals with embedded polyindole were successfully synthesized via precipitation, hydrothermal and in situ-polymerization strategy and hired for the removal of IMI from polluted water. The successful loading of PLN into these BNCs and efficient photo removal of IMI into harmless substances was depicted by FTIR. The UV-visible study showed the reduction in the band gap of the prepared composite from 2.38 to 2.13 eV on the deposition of polymer. SEM indicated the morphology and average particle size of 118 and 75 nm, respectively. XRD analysis measured crystal structure and average crystal size as 79 and 54 nm, respectively. Effect of numerous procedure parameters was premeditated and the optimized circumstances were pH 4, composite dose 0.05 g, pesticides concentration 6 mg, H_2O_2 dose 10 mM and contact time 60 min for PLN/CuO-NiO, Similarly, the optimized condition via PLN/Mn-Cu were pH 10, composite dose 0.05 g, IMI concentration 2 mg, H_2O_2 dose 10 mM, and illumination time 120 min and the order of degradation capacity was found to be 91 % and 98 % via the prepared composites,

Materials Advances Accepted Manuscript

respectively. A kinetic study demonstrated that the removal of IMI followed the BMG model using composites. The composite of CuO-NiO and Mn-Cu with PLN is efficient and could be used for catalytic removal of neonicotinoid insecticide IMI from polluted water and is also suitable for potential application in the remediation of other insecticides from effluents.

Declaration of competing interest

The authors declare that they have no known competing financial interests or personal relationships that could have appeared to influence the work reported in this paper.

References

1   H. Sukmana, N. Bellahsen, F. Pantoja and C. Hodur, *Prog. Agric. Eng. Sci.*, 2021, **17**, 49–68.

2   R. Akbar, H. N. Bhatti, M. Zahid and M. Y. Naz, *Environ. Sci. Pollut. Res.*, 2025, 1–25.

3   M. Lebiocka, .

4   M. A. Hassaan and A. El Nemr, *Egypt. J. Aquat. Res.*, 2020, **46**, 207–220.

5   P. Rezende-Teixeira, R. G. Dusi, P. C. Jimenez, L. S. Espindola and L. V Costa-Lotufo, *Environ. Pollut.*, 2022, **300**, 118983.

6   A. Intisar, A. Ramzan, T. Sawaira, A. T. Kareem, N. Hussain, M. I. Din, M. Bilal and H. M. N. Iqbal, *Chemosphere*, 2022, **293**, 133538.

7   M. P. Saini, *J. Healthc. LIFE-SCIENCE Res.*, 2023, **2**, 91–105.

8   L. Zuščíková, D. Bažány, H. Greifová, N. Knížatová, A. Kováčik, N. Lukáč and T. Jambor, *Toxics*, 2023, **11**, 598.

9   R. Guo, H. Zhang, C. Guo, N. Lv, B. Xi and J. Xu, *Chinese Chem. Lett.*, 2024, **35**, 109413.

10   M. Salemi and R. Brahimi, *Universite laarbi tebessi tebessa*, 2020.

11   Q. Kan, K. Lu, S. Dong, D. Shen, Q. Huang, Y. Tong, W. Wu, S. Gao and L. Mao, *Environ. Pollut.*, 2020, **267**, 115438.

12   H. Adabavazeh, A. Saljooqi, T. Shamspur and A. Mostafavi, *Polyhedron*, 2021, **198**,

Materials Advances Accepted Manuscript

Materials Advances Accepted Manuscript

115058.

13   M. Zangiabadi, A. Saljooqi, T. Shamspur and A. Mostafavi, *Ceram. Int.*, 2020, **46**, 6124–6128.

14   Q. Duan, S. Jiang, F. Chen, Z. Li, L. Ma, Y. Song, X. Yu, Y. Chen, H. Liu and L. Yu, *Ind. Crops Prod.*, 2023, **192**, 116075.

15   W. Kang, S. Chen, H. Yu, T. Xu, S. Wu, X. Wang, N. Lu, X. Quan and H. Liang, *J. Hazard. Mater.*, 2021, **405**, 124277.

16   A. Noor, S. R. M. Kutty, M. H. Isa, I. H. Farooqi, A. C. Affam, A. H. Birniwa and A. H. Jagaba, in *The treatment of pharmaceutical wastewater*, Elsevier, 2023, pp. 217–245.

17   N. Arora, A. Kumar and S. K. Singal, *Measurement*, 2022, **190**, 110700.

18   K. Harby, M. Emad, M. Benghanem, T. Z. Abolibda, K. Almohammadi, A. Aljabri, A. Alsaiari and M. Elgendi, *Desalination*, 2024, 117600.

19   O. Scialdone, F. Proietto and A. Galia, *Curr. Opin. Electrochem.*, 2021, **27**, 100682.

20   D. R. Lobato-Peralta, E. Duque-Brito, A. Ayala-Cortés, D. M. Arias, A. Longoria, A. K. Cuentas-Gallegos, P. J. Sebastian and P. U. Okoye, *J. Environ. Chem. Eng.*, 2021, **9**, 105626.

21   V. R. Moreira, R. N. Guimarães, P. B. Moser, L. V. S. Santos, E. C. de Paula, Y. A. R. Lebron, A. F. R. Silva, G. S. Casella and M. C. S. Amaral, *J. Water Process Eng.*, 2023, **51**, 103450.

22   A. Bibi, S. Bibi, M. Abu-Dieyeh and M. A. Al-Ghouti, *J. Clean. Prod.*, 2023, 137810.

23   J. Weng, J. Chen, Y. Xu, X. Hu, C. Guo, Y. Yang, J. Sun, L. Fu, Q. Wang and J. Wei, *J. Colloid Interface Sci.*, 2023, **652**, 1367–1380.

24   R. Biju, V. R. JR, R. Ravikumar and C. R. Indulal, *Plant Nano Biol.*, 2022, **2**, 100016.

25   M. Kumar, S. K. Samal and T. Maharana, *Polym. Technol. Mater.*, 2024, 1–20.

26   N. Chen, J. He, H. Xuan, J. Jin, K. Yu, M. Shi and C. Yan, *Compos. Part B Eng.*, 2024, **270**, 111145.

27   M. Atif Qaiyum, R. Kumari, J. Mohanta, P. P. Samal, S. Dutta, B. Dey and S. Dey, *J. Clust. Sci.*, 2023, **34**, 963–975.

28   C. Xie, L. Li, X. Zhai and W. Chu, *RSC Adv.*, 2023, **13**, 11069–11080.

29   L. Shao, P. Feng, Q. Liu, Y. Zhang, Z. Yu and S. Yan, *Constr. Build. Mater.*, 2024, **449**, 138294.

30   S. Ahmad, V. U. Siddiqui, A. Ansari, W. A. Siddiqi and M. K. Akram, in *AIP Conference Proceedings*, AIP Publishing, 2020, vol. 2276.

31   J.-R. Li, W.-P. Zhang, C. Li and C. He, *J. Colloid Interface Sci.*, 2021, **591**, 396–408.

32   S. Anandhi, M. L. Edward and V. Jaisankar, *Mater. Today Proc.*, 2021, **40**, S93–S101.

33   A. Nigam, B. Singh, S. Saini, A. K. Rai and S. J. Pawar, *Inorg. Nano-Metal Chem.*, 2023, 1–11.

34   M. N. Tahir, K. S. Munawar, M. Feizi-Dehnayebi, M. Ashfaq and M. E. Muhammed, *J. Mol. Struct.*, 2024, **1297**, 136956.

35   S. J. Mohammed, K. M. Omer and F. E. Hawaiz, *RSC Adv.*, 2023, **13**, 14340–14349.

36   Q. Wei, G. Zhang and J. Xie, *Food Hydrocoll.*, 2024, **149**, 109599.

37   S. Taherkhani, F. Ghamari, J. Arjomandi, A. Nasri and H. Shi, *Fuel*, 2023, **353**, 129167.

38   H. Humayun, B. Begum, S. Bilal, A. ul H. A. Shah and P. Röse, *Nanomaterials*, 2023, **13**, 618.

39   E. Arulkumar, S. S. Shree and S. Thanikaikarasan, *Results Chem.*, 2023, **6**, 101087.

40   H. C. Sathisha, G. Krishnamurthy, M. Pari, T. L. Soundarya and G. Nagaraju, *Elsevier*, 2023.

41   G. Zhou, Y. Chen, G. Chen, H. Xu, W. Yin, B. Wang, X. Zhu, X. Ning, P. K. Chu and X. Wang, *Appl. Catal. B Environ. Energy*, 2024, 124617.

42   N. O. Alafaleq, T. A. Zughaibi, N. R. Jabir, A. U. Khan, M. S. Khan and S. Tabrez, *Nanomaterials*, 2023, **13**, 1201.

43   Q. A. Alsulami and A. Rajeh, *Opt. Mater. (Amst).*, 2022, **123**, 111820.

44   E. Arulkumar and S. Thanikaikarasan, *Optik (Stuttg).*, 2024, **302**, 171685.

45   Z. Butt, M. Aamir, S. Aziz, J. Akhtar, A. Afaq, S. Naseer, Q. Wali, M. Nadeem and U. Jabeen, *Microsc. Res. Tech.*, 2023, **86**, 1132–1143.

46   Z. Nazeer, I. Bibi, F. Majid, S. Kamal, S. M. Ibrahim and M. Iqbal, *Opt. Mater. (Amst).*, 2022, **125**, 112090.

47   M. Alzaid, A. M. Abu-Dief, N. M. A. Hadia, M. Ezzeldien and W. S. Mohamed, *Opt. Quantum Electron.*, 2024, **56**, 1–22.

48   Z. U. Rahman, U. Shah, A. Alam, Z. Shah, K. Shaheen, S. B. Khan and S. A. Khan, *Inorg. Chem. Commun.*, 2023, **148**, 110312.

49   F. Lopresti, F. C. Pavia, M. Ceraulo, E. Capuana, V. Brucato, G. Ghersi, L. Botta and V. La Carrubba, *J. Biomed. Mater. Res. Part A*, 2021, **109**, 2120–2136.

50   M. Ateia, G. Ersan, M. G. Alalm, D. C. Boffito and T. Karanfil, *Environ. Sci. Process. Impacts*, 2022, **24**, 172–195.

51   M. Iqbal, H. N. Bhatti, S. Noreen and S. Shukrullah, *Environ. Sci. Pollut. Res.*, 2024, 1–31.

52   K. Sbissi, V. Collière, M. L. Kahn, E. K. Hlil, M. Ellouze and F. Elhalouani, *J. Nanostructure Chem.*, 2015, **5**, 313–323.

53   A. Solmaz, Ö. S. Bölükbaşi and Z. A. Sari, *Environ. Sci. Pollut. Res.*, 2024, **31**, 19795–

19814.

54   W. Giurlani, M. Innocenti and A. Lavacchi, *Coatings*, 2018, **8**, 84.

55   H. R. Barai, N. S. Lopa, F. Ahmed, N. A. Khan, S. A. Ansari, S. W. Joo and M. M. Rahman, *ACS omega*, 2020, **5**, 22356–22366.

56   H. Lv and H. Sun, *ACS omega*, 2020, **5**, 11324–11332.

57   M. Bin Mobarak, M. S. Hossain, F. Chowdhury and S. Ahmed, *Arab. J. Chem.*, 2022, **15**, 104117.

58   S. Sajjad, A. Ikhlaq, F. Javed, S. W. Ahmad and F. Qi, *Water Sci. Technol.*, 2021, **83**, 727–738.

59   A. Kausar, S. Ijaz, M. Rafaqat, A. Dahshan, A. A. Latif, S. Bibi, N. S. Al-Kadhi, S. A. Alissa, A. Nazir and M. Iqbal, *J. Mol. Liq.*, 2023, **391**, 123347.

60   Y. Cheng, Z. Wang, J. Wang, L. Cao, Z. Chen, Y. Chen, Z. Liu, P. Xie and J. Ma, *J. Hazard. Mater.*, 2023, **441**, 129885.

61   D. Kathuria, M. Bhattu, A. Bankar and P. Puri, *ChemistrySelect*, 2023, **8**, e202302293.

62   A. Iqbal, A. ul Haq, L. Rios-Aspajo and A. Iturriaga-Chavez, *Glob. NEST J.*, 2023, **25**, 150–158.

63   K. Bano, S. Kaushal, B. Lal, S. K. Joshi, R. Kumar and P. P. Singh, *Environ. Nanotechnology, Monit. Manag.*, 2023, **20**, 100863.

64   M. Ta, T. Wang, J. Guo, Y. Wang, J. Zhang, C. Zhao, S. Liu, G. Liu and H. Yang, *Sep. Purif. Technol.*, 2023, **310**, 123067.

65   Y. Zou, Y. Hu, Z. Shen, L. Yao, D. Tang, S. Zhang, S. Wang, B. Hu, G. Zhao and X. Wang, *J. Environ. Sci.*, 2022, **115**, 190–214.

66   M. Ortiz-Martínez, B. Restori-Corona, L. Hernández-García and D. Alonso-Segura, *Macromol*, 2024, **4**, 785–804.

67   S. Porcu, F. Secci and P. C. Ricci, *Molecules*, 2022, **27**, 6828.

68   C. Yang, H.-R. Yang, S.-S. Li, Q.-D. An, S.-R. Zhai and Z.-Y. Xiao, *J. Colloid Interface Sci.*, 2022, **625**, 651–663.

69   A. Iqbal, S. A. R. Naqvi, A. U. Haq and M. Saeed, *Authorea Prepr.*

70   Y. Yang, X. Ma, Z. Li, Y. Wang, C. Ju, L. Cao, Y. Zheng and Q. Zhang, *Chem. Eng. J.*, 2023, **465**, 142788.

71   R. Saleh, S. A. Hidayat, A. Taufik and S. Yin, *Arab. J. Chem.*, 2022, **15**, 103881.

72   S. Qu, H. Wu and Y. H. Ng, *Adv. Energy Mater.*, 2023, **13**, 2301047.

73   Y. Li, X. Gao and Y. Li, *Inorg. Chem. Front.*

74   M. N. Arifin, R. Jusoh, H. Abdullah, N. Ainirazali and H. D. Setiabudi, *Environ. Res.*,

2023, **229**, 115936.

75   F. Ma, Y. Wang, Z. Fu, Y. Tang, J. Dai, C. Li and W. Dong, *Constr. Build. Mater.*, 2022, **335**, 127494.

76   A. A. Fauzi, A. A. Jalil, N. S. Hassan, F. F. A. Aziz, M. S. Azami, T. A. T. Abdullah, M. F. A. Kamaroddin and H. D. Setiabudi, *Environ. Res.*, 2022, **211**, 113069.

77   H. Karimi-Maleh, M. Ghalkhani, Z. S. Dehkordi, J. Singh, Y. Wen, M. Baghayeri, J. Rouhi, L. Fu and S. Rajendran, *J. Ind. Eng. Chem.*, 2024, **129**, 105–123.

78   H. Shi, W. Wang, L. Mao, L. Zhang, L. Zhu, C. Wu and X. Liu, *J. Environ. Manage.*, 2025, **380**, 124929.

79   A. H. Zyoud, S. H. Zyoud and S. H. Zyoud, *Appl. Water Sci.*, 2025, **15**, 159.

80   W. Zhang, D. Liu, Z. Mu, X. Zhang, G. Dong, L. Bai, R. Guo, J. Li, M. Zhao and Z. Zhang, *J. Inorg. Organomet. Polym. Mater.*, 2023, **33**, 90–104.

81   R. Biju, R. Ravikumar, C. Thomas and C. R. Indulal, *J. Nanoparticle Res.*, 2022, **24**, 117.

82   A. D. Ali, S. H. Ammar and E. M. Khudhair, *Environ. Nanotechnology, Monit. Manag.*, 2020, **14**, 100359.

83   Y. T. Gaim, S. M. Yimanuh and Z. G. Kidanu, *J. Compos. Sci.*, 2022, **6**, 317.

84   M. Naghizadeh, M. A. Taher and A.-M. Tamaddon, *Heliyon*.

85   S. G. Mohammad and A. A. El-Refaey, *J. Water L. Dev.*, 2023, 220–230.

86   A. Khan, Z. A. Raza, H. N. Bhatti and T. Sarwar, *Int. J. Biol. Macromol.*, 2024, **261**, 129881.

87   A. G. A. Reyad, G. I. K. Marei, M. A. Abbassy, E. I. Rabea and M. E. I. Badawy, *Int. J. Mod. Agric. Environ.*, 2023, **3**, 29–48.

88   R. Juturu, V. R. Murty and R. Selvaraj, *Chemosphere*, 2024, **349**, 140731.

89   M. Tang, J. Wan, Y. Wang, Z. Yan, Y. Ma, J. Sun and S. Ding, *Chem. Eng. J.*, 2022, **445**, 136755.

90   X. Ji, Y. Liu, Z. Gao, H. Lin, X. Xu, Y. Zhang, K. Zhu, Y. Zhang, H. Sun and J. Duan, *Sep. Purif. Technol.*, 2024, **330**, 125235.

91   J. Kumar, P. Kaur, D. Sud, A. Saini and P. Bansal, *Mater. Today Proc.*, 2023, **78**, 849–857.

92   P. Butcherine, B. P. Kelaher and K. Benkendorff, *Aquat. Toxicol.*, 2022, **242**, 106050.

Materials Advances Accepted Manuscript

Data availability

The data used to support the findings of this study are available from the corresponding author upon request.

Materials Advances Accepted Manuscript